Free Radical Scavenging Activity of Chlorochalcones: An Integrated Computational and Experimental Study

Anita Dwi Puspitasari[1*], Maria Ulfah[1], Indah Hartati[2], Rissa Laila Vifta[3], Faris Hermawan[4], Munifilia Ekasari[5], and Lala Adetia Marlina[6]**

[1]*Faculty of Pharmacy, Universitas Wahid Hasyim, Semarang 50236, Indonesia*

[2]*Chemical Engineering Study Program, Faculty of Engineering, Universitas Wahid Hasyim, Semarang 50236, Indonesia*

[3]*Faculty of Pharmacy, Universitas Islam Sultan Agung, Semarang 50112, Indonesia*

[4]*Research Center for Pharmaceutical Ingredient and Traditional Medicine, National Research and Innovation Agency (BRIN), Serpong, 15354, Indonesia*

[5]*Chemistry Study Program, Universitas Jambi, Jambi, 36361, Indonesia*

[6]*Research Center for Computing, National Research and Innovation Agency (BRIN), Bandung 40135, Indonesia*

Corresponding author:

tel: +62-85226050501[*]; +62-81379567042[**]
email: anita@unwahas.ac.id[*]; lala002@brin.go.id[**]

Received: April 24, 2025
Accepted: July 28, 2025

DOI: 10.22146/ijc.106221

Abstract: *Chlorochalcone derivatives (chalcones 1–3) were synthesized using ultrasound-assisted Claisen-Schmidt condensation, yielding > 80%. Antioxidant activity was evaluated through DPPH and ABTS assays, demonstrating strong activity with IC_{50} values ranging from 61.52 ± 0.97 to 98.27 ± 1.42 ppm. Chalcones 1 and 2 show SPF potential at 40 ppm and chalcone 3 at 20 ppm (SPF 19.47 ± 0.46). ADMET analysis using the pkCSM tool confirmed favorable pharmacokinetic profiles and low toxicity, supporting their safety for potential applications. Additionally, density functional theory (DFT) calculations provided more profound insights into molecular stability and reactivity, including electronic properties such as HOMO-LUMO gaps, further corroborating their pharmacological efficacy. These results collectively indicate that chalcones 1–3 exhibit potent antioxidant activity, adequate UV protection, and promising pharmacokinetic properties. Integrating* in vitro, in silico, *and DFT analyses underscores their potential as multifunctional compounds for antioxidant and sunscreen applications.*

Keywords: *chalcone; ultrasound-assisted synthesis; antioxidant; sunscreen; DFT*

■ INTRODUCTION

Ultraviolet (UV) radiation is divided into three regions based on wavelength: UV-A (320–400 nm), UV-B (280–320 nm), and UV-C (200–280 nm). The ozone layer absorbs UV-C radiation, preventing it from reaching the Earth's surface. As a result, UV-A and UV-B are of primary concern for skin health due to their ability to penetrate the atmosphere and cause biological damage.

The UV-A, also called long-wave ultraviolet rays, has strong penetration capabilities, allowing it to pass through transparent materials like glass and plastics. Over 98% of UV-A rays from sunlight reach the Earth's surface after penetrating the ozone layer and clouds. These rays can deeply infiltrate the dermis, damaging elastic and collagen fibers and contributing to tanning and long-term skin damage. UV-A penetrates deeper into the dermis, degrading collagen and elastic fibers, leading to photoaging and indirect DNA damage via oxidative stress [1]. Due to its ability to deeply penetrate the skin and cause significant damage, protecting against UV-A rays in the 320–420 nm range is a critical priority [2].

UV-B, characterized by shorter wavelengths, is absorbed by glass, and the ozone layer blocks most UV-B rays, leaving less than 2% to reach the surface. UV-B rays are most intense during summer afternoons and play a role in vitamin D synthesis and mineral

metabolism. However, excessive exposure can result in tanning, erythema, redness, and peeling [3-4]. Studies have established that prolonged UV-B exposure increases the risk of skin cancer due to direct DNA damage by forming cyclobutane pyrimidine dimers (CPDs) [5]. Both types of UV radiation are implicated in skin carcinogenesis and necessitate effective photoprotection.

Sunscreens are a critical intervention for mitigating UV-induced damage. They are generally classified into physical and chemical sunscreens. Physical sunscreens, such as titanium dioxide (TiO_2) and zinc oxide (ZnO), scatter and reflect UV radiation, forming an immediate protective barrier [6-7]. Chemical sunscreens contain organic molecules that absorb UV radiation, converting it into non-damaging energy through photochemical processes [8-9]. However, the generation of reactive oxygen species (ROS) due to UV exposure remains a significant challenge, as these free radicals disrupt the skin's natural defense system. ROS have been shown to target collagen, elastin, and other structural proteins, leading to reduced skin elasticity, wrinkle formation, and increased skin cancer risk [10].

Chalcone derivatives have recently garnered attention for their dual role as UV absorbers and antioxidants. Chalcones, characterized by a 1,3-diphenylprop-2-en-1-one structure, are natural precursors to flavonoids and possess unique photoprotective and antioxidative properties. Their conjugated α,β-unsaturated carbonyl group allows effective UV absorption, while their phenolic groups neutralize free radicals through hydrogen donation [11-12]. Studies have demonstrated the potential of chalcones to protect against UV-A and UV-B damage. For example, Wijayanti et al. designed eight chalcone derivatives with high molar absorptivity in the UV range and promising sun protection factor (SPF) values, making them suitable candidates for sunscreen formulations [13].

Research has also explored the antioxidant activities of chalcones. Zainuri et al. [14] synthesized chalcone derivatives with fused anthracene rings, demonstrating excellent free radical scavenging abilities and UV protective properties. Similarly, Głębocka et al. [15] used density functional theory (DFT) to model the stability of chalcone isomers, showing that structural modifications could significantly enhance their photoprotection and antioxidative efficacy. Additionally, Wachter et al. confirmed through DFT calculations that the trans isomer of chalcones is more stable and better suited for UV protection than the cis isomer due to reduced steric hindrance [16].

Advancements in synthetic methods have facilitated the development of chalcones with enhanced properties. Ultrasound-assisted synthesis has emerged as a green chemistry approach, significantly reducing reaction times and increasing yields [17-18]. For instance, Tri Suma et al. synthesized *p*-chlorochalcones using ultrasonic waves, achieving reaction times as short as 0.9–4.2 h compared to longer reaction times (1.75–26.5 h) with conventional methods. These findings underscore the potential of chalcones in sustainable chemical applications and their adaptability for various industrial uses [17].

Integrating chalcones into photoprotection research also benefits from the synergy between experimental and computational studies. Experimental methods provide empirical data on efficacy and mechanisms, while computational approaches like DFT offer predictive insights into molecular behavior. Together, these strategies enhance the design of chalcone derivatives for sunscreen formulations, as studies link chalcone structures to their ability to absorb specific UV wavelengths [13]. The design of active sunscreen agents is crucial for mitigating UV-induced damage. Recent research on (3*E*,5*E*)-3,5-dibenzylidene-1-methylpiperidin-4-one derivatives highlights the impact of halogen substituents on UV absorbance, reactivity, and optical properties. Computational analyses showed strong UV absorption peaks (300–320 nm) covering UV-A and UV-B regions, with high molar absorptivity and promising reactivity at key molecular sites. Halogen substitution enhanced their protective and optical properties, while their simple synthesis makes them promising candidates for experimental validation in sunscreen and optoelectronic applications [19].

Chalcones represent a versatile and promising class of compounds for addressing UV-induced skin damage, offering dual-action properties as UV absorbers and antioxidants. These characteristics position

chalcones as strong candidates for multifunctional applications in cosmetics and pharmaceuticals, with research advancements continually expanding their potential. This study focuses on chlorochalcone derivatives, investigating their properties through experimental techniques and theoretical calculations. DFT calculations were used to explore their electronic, energetic, and structural features. By integrating experimental and computational methods, this research provides valuable insights into the physicochemical behavior of chlorochalcones, emphasizing their potential for innovative and sustainable solutions in photoprotection.

■ EXPERIMENTAL SECTION

Materials

The chemicals utilized in this study were of pro-analytical grade and used without further purification. The synthesis of chalcone was performed using benzaldehyde, 2-chlorobenzaldehyde, 4-chlorobenzaldehyde, 2-chloroacetophenone, methanol, ethanol, chloroform, hydrochloric acid (HCl), sodium hydroxide (NaOH), and thin-layer chromatography (TLC) plates (silica gel 60 F254). For the antioxidant and sunscreen activity assessments, key reagents included 2,2'-azinobis(3-ethylbenzothiazoline-6-sulfonic acid) (ABTS), 2,2-diphenyl-1-picrylhydrazyl (DPPH), Trolox, ascorbic acid, and potassium persulfate. All chemicals were purchased from Merck.

Instrumentation

Structural elucidations were performed using a TLC scanner (CAMAG TLC-Scanner 3), gas chromatography-mass spectrometer (GC-MS, Shimadzu QP2010S), Fourier Transform Infrared spectrophotometer (FTIR, Shimadzu Prestige 21), a nuclear magnetic resonance (NMR) spectrometer (JEOL JNM-ECA500, ^{1}H at 500 MHz and ^{13}C at 125 MHz), and UV-vis spectrophotometer (Shimadzu UV-1800).

Procedure

Chlorochalcone synthesis

The reaction scheme, illustrated in Scheme 1, involved the coupling of aromatic aldehydes and ketones under basic conditions. An ultrasound-assisted method followed a previously reported protocol with slight modifications [20]. A solution of aqueous methanol-sodium hydroxide (10 mL water, 10 mL methanol, 5% NaOH) was prepared in an Erlenmeyer flask and placed in an ultrasonic cleaner water bath. To this solution, 5 mmol of 2-chloroacetophenone was added, and the mixture was sonicated for 5 min to promote dissolution and initial reaction. Subsequently, 5 mmol of the appropriate benzaldehyde was introduced to the reaction mixture, and sonication was continued at room temperature. Reaction progress was monitored using thin-layer chromatography (TLC) at 10 min intervals to determine the optimal reaction time. After completing the sonication process, the flask was stored in a refrigerator for 24 h to allow the product to crystallize. The resulting solid was filtrated and dried to remove residual solvents and impurities. The crude product was purified using ethanol as the solvent through recrystallization. A conventional method followed a previously reported protocol with slight modifications [20]. A solution of aqueous methanol-sodium hydroxide (10 mL water, 10 mL methanol, 5% NaOH) was prepared in an Erlenmeyer flask. This solution added 5 mmol of 2-chloroacetophenone, and the mixture was stirred for 5 min to promote dissolution and initial reaction. Subsequently, 5 mmol of the appropriate benzaldehyde was introduced to the reaction mixture, and stirring was continued at room temperature. Reaction progress was

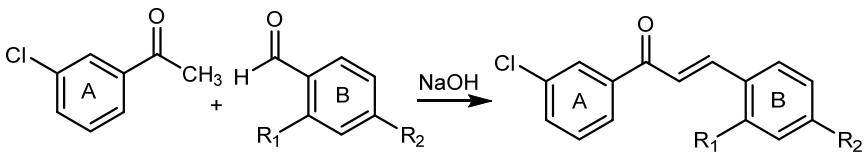

1. R_1 = H, R_2 = H
2. R_1 = Cl, R_2 = H
3. R_1 = H, R_2 = Cl

Scheme 1. Reaction scheme for chalcones 1–3 synthesis

monitored using TLC at 10-min intervals to determine the optimal reaction time. After the stirring process, the flask was stored in a refrigerator for 24 h to allow the product to crystallize. The resulting solid was filtrated and dried to remove residual solvents and impurities. The crude product was purified using ethanol as the solvent through recrystallization.

Chalcone 1: (*E*)-1-(3-chlorophenyl)-3-phenylprop-2-en-1-one. IR (KBr): 3053 (Csp^2-H), 1667 (C=O), 1615 & 1568 (Ar C=C), 1039 (Ar C–Cl), 987 (*trans* Csp^2-H bend.) cm^{-1}; ^{1}H-NMR ($CDCl_3$, δ): 7.43 (3H, *m*, ArH), 7.42 (1H, *d*, *J* = 16 Hz, =C-Hα), 7.53 (1H, *s*, ArH), 7.58 (1H, *dq*, *J* = 1.5, 7.5 Hz, ArH), 7.62 (2H, *m*, ArH), 7.82 (1H, *d*, *J* = 17 Hz, =C-Hβ), 7.90 (1H, *dt*, *J* = 2.5, 7 Hz, ArH), 7.99 (1H, *t*, *J* = 2 Hz, ArH); ^{13}C-NMR ($CDCl_3$, δ): 189.24 (C=O), 145.81 (C=C), 139.87, 135.03, 134.69 (CAr), 132.81, 130.95, 130.06, 129.12, 128.67, 126.65 (9 CHAr), 121.51 (C=C); Mass spectrum (EI): *m/z* 244 (M^{+2}, ^{37}Cl); m.p. 98.2–99.8 °C; a light-yellow crystal.

Chalcone 2: (*E*)-1,3-bis(2-chlorophenyl)prop-2-en-1-one. IR (KBr): 3070 (Csp^2-H str.), 2924 (Csp^3-H str.), 1666 (C=O), 1604 (Ar C=C), 1201, 1059 (C–O), 980 (*trans* Csp^2-H bend.), 758 (Ar C–Cl) cm^{-1}; ^{1}H-NMR ($CDCl_3$, δ): 7.12 (1H, *d*, *J* = 17 Hz, =C-Hα), 7.33 (3H, *m*, ArH), 7.39 (1H, *dd*, *J1* = 7 Hz *J2* = 2 Hz, ArH), 7.42 (2H, *m*, ArH), 7.51 (1H, *dd*, *J1* = 7.5 Hz *J2* = 1.5 Hz, ArH), 7.67 (1H, *dd*, *J1* = 8 Hz *J2* = 2.5 Hz, ArH), 7.86 (1H, *d*, *J* = 17 Hz, =C-Hβ). ^{13}C-NMR ($CDCl_3$, δ): 193.68 (C=O), 141.94 (=Cβ), 138.86 (CAr), 135.59 (CHAr), 132.79, 131.74, 131.65 (3CAr), 131.47, 130.44, 130.35, 129.6, 128.51, 127.91, 127.29 (7CHAr), 126.99 (=Cα); Mass spectrum (EI): *m/z* 276 (M^+); m.p. 50.3–51.9 °C; a pale-yellow crystal.

Chalcone 3: (*E*)-1-(3-chlorophenyl)-3-(4-chlorophenyl)prop-2-en-1-one. IR (KBr): 3070 (Csp^2-H str.), 1658 (C=O), 1602 (Ar C=C), 1211 (O–C–O), 980 (trans Csp^2-H bend.), 826 (Ar C–Cl) cm^{-1}; ^{1}H-NMR ($CDCl_3$, δ): 7.35 (2H, *dt*, *J1* = 9.5 Hz *J2* = 2.5 Hz, ArH), 7.45 (1H, *d*, *J* = 15.5 Hz, =C-Hα), 7.47 (1H, *t*, *J* = 7.5 Hz, ArH), 7.59 (3H, *m*, ArH), 7.77 (1H, *d*, *J* = 16 Hz, =C-Hβ), 7.88(1H, *dt*, *J1* = 7.5 Hz *J2* = 1.5 Hz, ArH), 7.98 (*t*, *J* = 4 Hz, ArH). ^{13}C-NMR ($CDCl_3$, δ): 188.93 (C=O), 144.26 (=Cβ), 139.67, 136.86 (2CAr), 135.07 (CHAr), 133.16, 132.95 (2CAr), 130.12, 129.81, 129.42, 128.66, 126.64 (7CHAr), 121.85 (=Cα); Mass spectrum (EI): *m/z* 276 (M^+); m.p. 133.4–135.2 °C; a pale-yellow crystal.

Antioxidant activity test

The chalcones were evaluated for their in vitro antioxidant capacities using two well-established methods: the DPPH assay, with ascorbic acid as the reference antioxidant, and the ABTS assay, with Trolox as the reference antioxidant. The antioxidant activities of the chalcones were assessed across a concentration range of 20–100 μg/mL. Dose-response curves for each compound were generated and analyzed using linear regression to calculate the half-maximal inhibitory concentration (IC_{50}), representing the concentration required to achieve 50% radical scavenging activity.

DPPH method. The antioxidant activity of the chalcones was evaluated using the DPPH free radical scavenging method. A DPPH stock solution (1.3 mg/mL) was prepared in ethanol. From this solution, 100 μL was diluted with 3 mL of ethanol to prepare the working DPPH solution. The chalcones were prepared as test solutions in five concentrations: 20, 40, 60, 80, and 100 ppm. Ascorbic acid, used as the standard, was prepared in a similar series of five concentrations: 2, 4, 6, 8, and 10 ppm. For each sample, 1 mL of the respective solution was taken, diluted with 3 mL of ethanol, and mixed with 100 μL of the working DPPH solution. The mixtures were left to react in the dark for 30 min to ensure adequate interaction between the DPPH radical and the antioxidants in the test solutions. Following this incubation period, the absorbance of each mixture was measured at 516 nm using a UV-vis spectrophotometer.

ABTS method. The antioxidant activity of the chalcones was assessed using the ABTS radical scavenging assay. To prepare the ABTS working solution, 7 mg of ABTS and 3.5 mg of potassium persulfate were dissolved in 25 mL of aqua pro injection. The solution was incubated in the dark at room temperature for 12 h to allow the formation of ABTS radicals. Chalcone samples were prepared in five concentrations: 20, 40, 60, 80, and 100 ppm. A Trolox solution, serving as the standard antioxidant, was prepared in five concentrations: 5, 10, 15, 20, and

25 ppm. For each test, 1 mL of the chalcone or standard solution was taken, diluted with 3 mL of ethanol, and mixed with 1 mL of the prepared ABTS solution. The mixtures were left to stand in the dark for 30 min to ensure complete interaction between the ABTS radicals and the antioxidant compounds. After the incubation period, the absorbance of each sample was measured at a wavelength of 734 nm using a UV-vis spectrophotometer.

In vitro *sunscreen activity*

Chalcone solutions were initially prepared in ethanol at a concentration of 1000 ppm. These stock solutions were then serially diluted to obtain 10, 20, 30, 40, and 50 ppm concentrations. The UV absorbance of each solution was measured using a UV-vis spectrophotometer across a wavelength range of 290–320 nm to determine their SPF values.

The transmission percentage (%Te) was calculated in the wavelength range of 292.5–317.5 nm, and the percentage of transmitted ultraviolet radiation (%Tp) was determined in the 322.5–372.5 nm range. Measurements were taken at 5 nm intervals. All tests were conducted in triplicate for each concentration to ensure reliability and reproducibility.

The sun protection factor (SPF) values were calculated using the Mansur equation presented in Eq. (1), which integrates the absorbance data and the erythemal effectiveness spectrum (EE × I) values. These EE × I constants were obtained from the method outlined by Sayre et al. [21]. For comparison, benzophenone-3, a standard sunscreen agent, was prepared and tested following the same protocol as the chalcone samples.

$$SPF = CF \times \Sigma EE(\lambda) \times I(\lambda) \times abs(\lambda) \quad (1)$$

where CF is the correction factor, EE(λ) is the erythmogenic effect of radiation with wavelength λ, I(λ) is the sun intensity spectrum at wavelength λ, and abs(λ) is the spectrophotometric absorbance value at wavelength λ. The percentage transmittance of erythema (%Te) was calculated based on the transmittance value at a wavelength of 292.5–317.5 nm, while the percentage transmittance of pigmentation (%Tp) was calculated at 322.5–372.5 nm. The percentage transmittance of erythema and pigmentation was calculated using Eq. (2).

$$\%Te = \frac{Ee}{\Sigma Fe} \text{ and } \%Tp = \frac{Ep}{\Sigma Fp} \quad (2)$$

where Fe is erythema flux, Fp is pigmentation flux, Ee can be defined as the amount of erythema flux transmitted by the sample at the wavelength range and calculated as Ee = ΣT × Fe, where T is the transmittance. Ep can be defined and calculated in a similar way to Ee.

Quantum chemical calculations

Quantum-chemical DFT calculations of chlorochalcone derivatives were performed using the Gaussian 09 software package [22]. The M06-2X functional [23] was used in conjunction with Pople's 6–311G(*d*,*p*) basis set [24]. The molecular electrostatic potential (MEP) was computed at the M06-2X/6-311++G(*d*,*p*) level of theory in the gas phase for each chalcone, and the isosurfaces were generated using an isovalue of 0.02 electrons/A^3.

The three primary antioxidant mechanisms discussed in the literature [25-27] are hydrogen atom transfer (HAT), single electron transfer-proton transfer (SET-PT), and sequential proton loss electron transfer (SPLET). The HAT mechanism occurs when a free radical species ($R^{\bullet}$) reacts with an antioxidant molecule, abstracting a hydrogen atom from the antioxidant (Eq. (3)). In the SET-PT mechanism, a two-step process occurs. First, a free radical species removes an electron from the antioxidant molecule (HX), generating a cation radical ($HX^{+\bullet}$), which is followed by a proton transfer to stabilize the system (Eqs. (4) and (5)). The SPLET mechanism begins with the antioxidant molecule losing a proton (H^+) to form an anionic species (X^-), which subsequently transfers an electron to the free radical species (Eqs. (6) and (7)). It is well-established in the literature that these mechanisms can occur simultaneously, albeit at different rates, depending on the specific conditions and molecules involved [25-27].

$$R^{\bullet} + HX \rightarrow RH + X^{\bullet} \quad (3)$$

$$R^{\bullet} + HX \rightarrow R^- + HX^{+\bullet} \quad (4)$$

$$R^- + HX^{+\bullet} \rightarrow RH + X^{\bullet} \quad (5)$$

$$HX \rightarrow X^- + H^+ \quad (6)$$

$$X^- + R^{\bullet} \rightarrow X^{\bullet} + R^- \quad (7)$$

The reactivity of antioxidants in the three mechanisms—HAT, SET-PT, and SPLET—can be quantified through specific thermodynamic parameters. In the HAT mechanism, the bond dissociation energy (BDE, Eq. (8)) of the H–X bond in the antioxidant species, where X represents a carbon atom, is the key determinant of reactivity. A lower BDE value indicates a higher antioxidant reactivity [25]. For the SET-PT mechanism, reactivity is calculated as the sum of the ionization potential (IP, Eq. (9)) and the proton dissociation enthalpy (PDE, Eq. (10)). Lower values of IP and PDE correspond to greater antioxidant reactivity [25]. In the SPLET mechanism, reactivity is evaluated through the proton affinity (PA, Eq. (11)) of the anionic form of the antioxidant molecule (X^-) and the electron transfer enthalpy (ETE, Eq. (12)), which measures the energy required to transfer an electron from the anionic species (X^-) to the free radical ($R^\bullet$). Lower PA and ETE values indicate higher reactivity in this mechanism [25]. These parameters collectively provide insights into the efficiency of antioxidants in mitigating free radical damage through these mechanisms.

$$BDE = H(X^\bullet) + H(H^\bullet) - H(XH) \quad (8)$$

$$IP = H(HX^{+\bullet}) + H(e^\bullet) - H(XH) \quad (9)$$

$$PDE = H(X^\bullet) + H(H^+) - H(X^{+\bullet}) \quad (10)$$

$$PA = H(X^-) + H(H^+) - H(XH) \quad (11)$$

$$ETE = H(X^\bullet) + H(e^\bullet) - H(X^-) \quad (12)$$

The H notations in Eqs. (8–12) stands for the calculated enthalpy of the species in the parentheses.

The optimized geometries of the cation radical ($HX^{+\bullet}$), the neutral radical ($X^\bullet$), and the anionic species (X^-) were calculated using the M06-2X functional with the 6-311++G(*d*,*p*) basis set. Water was employed as the implicit solvent within the conductor polarizable continuum model (CPCM) method [28-29], and all calculations were performed under standard conditions of 298.15 K temperature and 1 atm pressure. The enthalpy values for the hydrogen atom ($H^\bullet$), proton (H^+), and electron (e^-) were adopted from the works of Rimarčík et al. [30] and Szeląg et al. [31], ensuring the thermodynamic consistency for the calculations.

Global quantum reactivity descriptors were calculated using Eqs. (13–20) to assess the chemical reactivity and stability of the chalcones and the chemical reactivity of the chalcones. These include the HOMO-LUMO energy gap (ΔE_{H-L}), which indicates stability and reactivity, ionization potential (IP) and electron affinity (EA), reflecting electron donation and acceptance capabilities, and electronegativity (χ), showing electron attraction tendency. Global hardness (η) and global softness (σ) describe resistance to deformation and polarizability, while the global electrophilicity index (ω) and global nucleophilicity index (ε) assess the molecule's ability to accept or donate electrons. These parameters collectively offer a detailed profile of the chalcones' electronic properties and reactivity [32-33].

$$\Delta E_{H-L} = E_{LUMO} - E_{HOMO} \quad (13)$$

$$IP = -E_{HOMO} \quad (14)$$

$$EA = -E_{LUMO} \quad (15)$$

$$\chi = \frac{I + A}{2} \quad (16)$$

$$\eta = \frac{I - A}{2} \quad (17)$$

$$\sigma = \frac{1}{\eta} \quad (18)$$

$$\omega = \frac{\chi^2}{2\eta} \quad (19)$$

$$\varepsilon = \frac{1}{\omega} \quad (20)$$

Adsorption, distribution, metabolism, excretion, and toxicity prediction

The selected compounds' SMILES were input into the pkCSM predictor [34], which can predict the pharmacokinetic properties of small molecules using graph-based signatures (http://biosig.unimelb.edu.au/pkcsm/). This dynamic tool is continuously updated with experimental data to predict multiple ADMET-related properties—Absorption, Distribution, Metabolism, Excretion, and Toxicity—simultaneously. The quantitative data provided by pkCSM was converted into binary data based on predefined thresholds [35]. These binary vectors, which represent the ADMET characteristics of each compound, were then compiled into a matrix and used as input for GenePattern to perform hierarchical clustering, using Euclidean distance and average linkage as the parameters.

■ RESULTS AND DISCUSSION

Synthesis of Chalcone 1–3

The synthesis results of chalcones 1–3 using ultrasound-assisted methods are presented in Table 1. This method demonstrated excellent efficiency, yielding products with high yields (> 80%) in significantly reduced reaction times. The application of acoustic energy contributed to accelerating the reaction process by enhancing molecular interactions and energy transfer. These results highlight the effectiveness of ultrasound-assisted synthesis in improving reaction efficiency and overall productivity compared to conventional methods.

Sunscreen Activity

Evaluating sunscreen potential involved calculating the SPF, %Te, and %Tp. The SPF value is a critical metric to assess a compound's ability to protect skin from harmful UV radiation. It indicates how often an individual's natural skin resistance to sunburn is enhanced when using sunscreen [36]. The SPF values of compounds can be classified into four categories: minimal protection for SPF values below 2, moderate protection for SPF values between 2–11, maximum protection for SPF values between 12–30, and ultra protection for SPF values exceeding 30 [37].

As shown in Fig. 1, chalcone 1 achieves ultra protection at 50 ppm, whereas chalcones 2 and 3 demonstrate ultra protection at a lower concentration of 40 ppm, indicating superior efficacy. In contrast, benzophenone, used as the control, provides only moderate protection at a concentration of 50 ppm. These results highlight the potential of chalcones, particularly chalcones 2 and 3, as effective sunscreen agents with significant UV-blocking properties. The higher protection observed at lower concentrations for chalcones 2 and 3 suggests that their structural features, such as substituent position and electronic effects, may enhance their ability to absorb or reflect UV radiation efficiently.

Skin erythema can be externally triggered by exposure to electromagnetic waves, including UV, visible light, and infrared radiation [38]. To evaluate the sunscreen activity of a compound, its ability to mitigate erythema and pigmentation can be categorized based on %Te and %Tp

Table 1. Optimization of the formation of the chalcones

Chalcone	Method			
	Ultrasound		Conventional	
	Time (h)	Yield (%)	Time (h)	Yield (%)
1	1.33	82.8	13	76.5
2	0.92	83.4	8	77.9
3	1.17	80.9	11	69.8

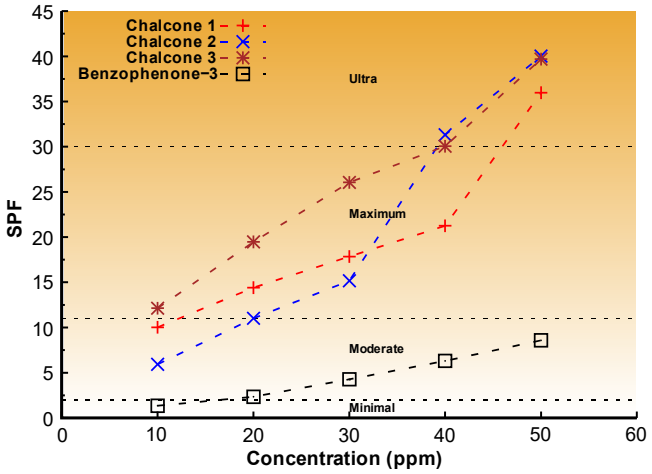

Fig 1. SPF values of the synthesized compounds compared to the benzophenone control as a function of concentration

at various concentrations. These parameters indicate how effectively a compound blocks or reduces the transmission of harmful radiation. The analysis of sunscreen activity for chalcones 1–3 was conducted by grouping their activity based on %Te and %Tp values, which reflect their UV absorption and skin-protective potential. The results of this analysis, highlighting the sunscreen activity categories of the chalcones, are presented in Fig. 2.

Sunscreen potential is categorized based on %Te and %Tp values as follows: sunblock (%Te < 1% and (%Tp = 3–40%), extra protection (%Te = 1–6% and %Tp 42–86%), suntan (%Te = 6–12% and %Tp = 45–86%), and fast tanning (%Te = 10–18% and %Tp = 45–86%) [39]. The sunblock category represents the highest level of protection, where compounds can effectively shield the skin from both UV-A and UV-B [40]. Our study used benzophenone-3 as a control compound due to its well-documented, predictable erythema and pigmentation responses to UV exposure, ensuring that our %Te and

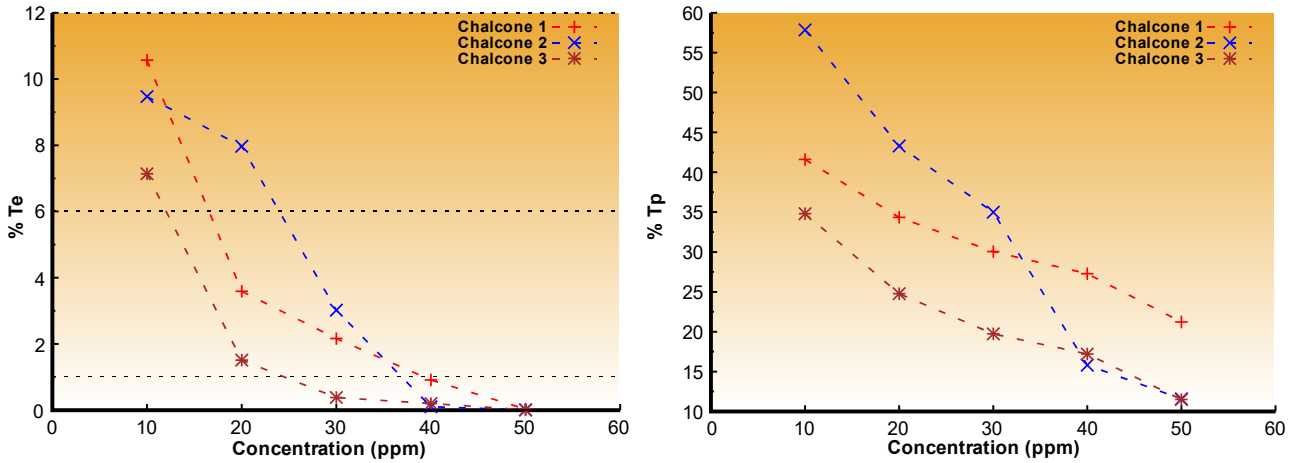

Fig 2. The percentage of erythema transmission (%Te) and % pigmentation transmission (%Tp) values of the synthesized compounds as a function of concentration

%Tp results were accurate and reliable (Table S1). As shown in Fig. 2, chalcones 1 and 2 achieve the sunblock category at 40 ppm, demonstrating their strong potential to protect the skin from harmful UV radiation fully. Notably, chalcone 3 exhibits even greater efficacy, entering the sunblock category at a lower concentration of 20 ppm. These results highlight the significant sunscreen potential of these chalcones, particularly chalcone 3, which may be attributed to their superior structural and photoprotective properties.

Sunscreen activity is related to the UV-vis absorption of the molecules. We have theoretically determined the chalcones' electronic transition energies and corresponding oscillator strengths using TD-DFT/M06-2X/6-311++G(*d*,*p*) calculations based on ground-state optimized geometries in water solution. The simulated UV-vis spectra are illustrated in Fig. 3. The calculated absorption wavelengths with the highest oscillator strengths are 310.68, 303.64, and 313.87 nm for chalcone 1, 2, and 3, respectively, indicating strong absorption within the UV-B range. Notably, these calculated values align closely with experimental results, confirming the reliability of our electronic spectral calculations for these flavonoids. Additionally, the absorption wavelengths for chalcone 3 are red-shifted compared to the others, consistent with the reduced energy gap. Our theoretical findings suggest that increasing the number of chlorine groups on flavonoids could effectively induce red-shifted electronic spectra, providing valuable insights for spectral tuning.

Antioxidant Activity

The IC_{50} values for the chalcones, determined from the DPPH and ABTS assays, are summarized in Table 2. Based on IC_{50} values, antioxidant activity is classified as

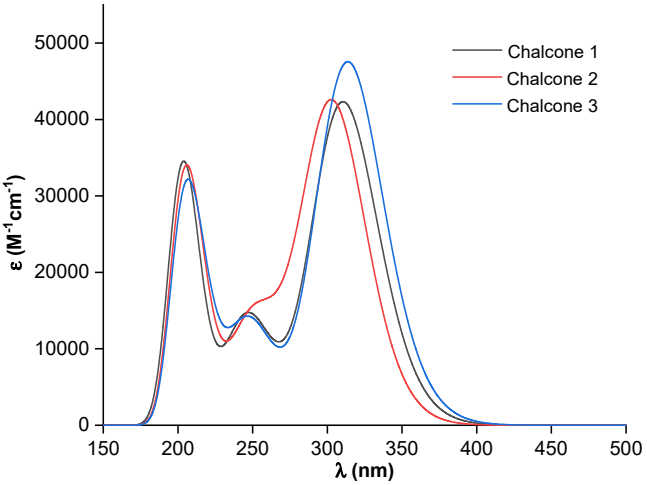

Fig 3. Simulated UV–vis absorption spectra in the water solution of chalcones 1–3

Table 2. Antioxidant activity of chalcones 1–3 using DPPH and ABTS method

Compound	IC_{50} (ppm)	
	DPPH	ABTS
Trolox	-	19.49 ± 0.34
Ascorbic acid	7.21 ± 2.11	-
Chalcone 1	92.77 ± 1.21	78.68 ± 3.35
Chalcone 2	98.27 ± 1.42	81.45 ± 2.56
Chalcone 3	81.48 ± 0.69	61.52 ± 0.97

strong for IC_{50} < 50 ppm, strong for IC_{50} between 50–100 ppm, moderate for IC_{50} between 100–150 ppm, and weak for IC_{50} > 150 ppm [41]. Table 2 demonstrates that the chalcones exhibit high antioxidant activity, falling within the "strong" categories. Among the tested compounds, the substitution pattern of the chloro-group significantly influences antioxidant efficacy. Chalcone 3, with a chloro substituent in the para position, displays superior antioxidant activity compared to chalcone 2, which has the chloro group in the ortho position. This suggests that the para-substitution enhances radical scavenging capacity, potentially due to electronic or steric effects that improve interaction with free radicals.

To complement the experimental antioxidant activity of the studied chalcones, the possible radical scavenging mechanism was assessed using quantum chemical calculations. There are three primary antioxidant mechanisms: HAT, SET-PT, and SPLET. The calculated descriptor values, derived from reaction enthalpies, are presented in Table 3. A particular mechanism is deemed favorable for the compound when its associated parameters are relatively low, signifying its suitability for its antioxidant action. The chalcones' molecular structure and atomic numbering are shown in Fig. 4.

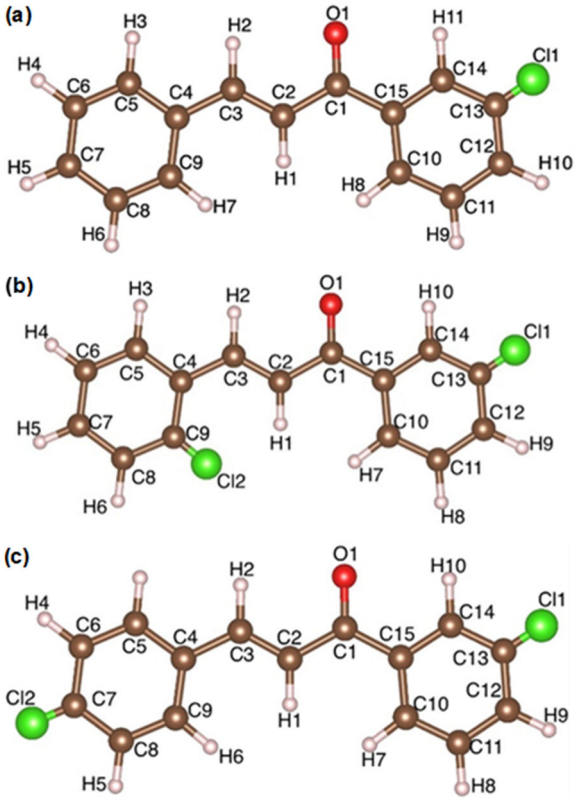

Fig 4. Molecular structure and atomic numbering of (a) chalcone 1, (b) chalcone 2, and (c) chalcone 3

The HAT Mechanism

Previous studies have highlighted the importance of the BDE value in evaluating the antioxidant activity of chemical substances. BDE is a key parameter associated with the HAT mechanism. The BDE value reflects a compound's ability to donate a hydrogen radical and form a stable donor radical. Thus, a lower BDE value signifies stronger antioxidant properties [42-43].

Analysis of the HAT mechanism for the compound identified the C–H site as the most favorable for radical formation in the gas phase, possessing the lowest BDE. This makes the C–H BDE a crucial factor in evaluating the antioxidant potential of phenolic substances, as the strength of the C–H bond determines the efficiency of hydrogen radical abstraction. The C–H BDE has a direct linear relationship with its activation energy, indicating that lower C–H BDE values correspond to lower activation energies and more prominent hydrogen abstraction potential [44].

To identify the weakest bond in both compounds, BDE calculations were conducted for all possible C–H bond dissociations. Chalcone 3 contains eight C–H bonds, with BDE values ranging from 109.03 to 156.66 kcal mol^{-1}, as detailed in Table 3. The C3–H2 bond shows the lowest BDE (109.03 kcal mol^{-1}), which can be attributed to the extensive delocalization of the radical formed at this site. A conjugated double-bond system creates a resonance effect that allows the unpaired electron on the C3 radical to disperse across the molecule, increasing its stability.

The C2–H1 bond also has a competitive BDE value, making chalcone 3 particularly reactive due to its dual active sites. In contrast, the higher BDE value is observed for the C14–H10 bond, likely due to intramolecular hydrogen bonding with a neighboring carbonyl group. Compared to previously studied chalcone derivatives [30,45], Chalcone 3 demonstrates strong antioxidant potential with notable activity at its two reactive sites. The formation of stable radicals after

Table 3. The BDE, IP, PDE, PA and ETE values in kcal mol^{-1} for the chalcones

Chal.	IP	Bonds	BDE	PDE	PA	ETE
1	168.10	C2–H1	109.30	253.06	319.44	101.72
		C3–H2	108.71	252.47	332.05	88.53
		C5–H3	112.40	256.16	340.35	83.91
		C6–H4	111.67	255.43	343.07	80.47
		C7–H5	111.58	255.34	341.23	82.21
		C14–H11	159.88	303.64	331.33	140.41
		C12–H10	161.04	304.80	330.75	142.15
		C11–H9	112.78	256.54	336.42	88.22
		C10–H8	159.45	303.21	333.77	137.54
2	168.37	C2–H1	103.07	246.56	318.09	96.85
		C3–H2	102.85	246.34	326.19	88.53
		C5–H3	111.69	255.18	335.52	88.03
		C6–H4	113.11	256.60	338.87	86.10
		C7–H5	112.79	256.28	336.53	88.13
		C8–H6	112.84	256.33	330.97	93.74
		C14–H10	115.08	258.58	330.30	96.65
		C12–H9	113.32	256.81	330.05	95.13
		C11–H8	112.22	255.71	336.40	87.69
		C10–H7	110.69	254.18	333.00	89.56
3	169.00	C2–H1	109.43	252.30	319.17	102.13
		C3–H2	109.03	251.89	331.09	89.80
		C5–H3	112.38	255.24	335.13	89.11
		C6–H4	156.66	299.53	330.76	137.76
		C14–H10	159.27	302.14	331.15	139.98
		C12–H9	113.89	256.75	330.57	95.18
		C11–H8	112.21	255.08	337.52	86.56
		C10–H7	110.94	253.81	332.92	89.89

hydrogen loss further supports the enhanced antioxidant efficiency of chalcone 3. These results indicate that its low BDE values and effective radical stabilization contribute to its superior antioxidant properties compared to other chalcones.

The SET-PT Mechanism

This mechanism involves two key stages: ionization and proton dissociation. In the ionization phase, an antioxidant molecule loses an electron, forming a radical cation. In the subsequent dissociation step, the radical cation undergoes deprotonation, producing a radical form of the antioxidant species and a free proton [46-47].

SET-PT mechanism is governed by two primary parameters: ionization potential (IP) and proton dissociation enthalpy (PDE). In the first step of this process, the antioxidant molecule (HX) donates an electron to the free radical species ($R^{\bullet}$), resulting in the formation of a radical cation ($HX^{+\bullet}$) and an anion (R^{-}) (Eq. (4)). This electron donation is influenced by the IP value, where a lower IP enhances the molecule's electron-donating ability.

In the second step, a proton is transferred from the radical cation ($HX^{+\bullet}$) to R^{-}, producing RH and a neutral antioxidant radical ($X^{\bullet}$) (Eq. (5)). The efficiency of this step depends on the PDE, with lower PDE values indicating a more favorable proton transfer due to the stabilization of the resulting radical.

The sum of IP and PDE determines the overall antioxidant reactivity within the SET-PT mechanism, where lower combined values correspond to higher antioxidant efficiency. Table 3 presents the calculated IP and PDE values, providing an in-depth view of antioxidant performance under this mechanism. The data reveal that IP values are generally higher than the BDE values, indicating that the SET-PT mechanism is less favorable than the HAT mechanism when only considering IP. However, it is essential to thoroughly consider PDE values to compare these mechanisms. Lower PDE values correspond to the formation of more stable radicals. Overall, the combined IP and PDE values (IP + PDE) for the SET-PT mechanism tend to be higher than the BDE values for the HAT mechanism, reinforcing that the SET-PT pathway is generally less favorable than the HAT mechanism.

The SPLET Mechanism

The SPLET mechanism begins with the deprotonation of antioxidant molecules, leading to the formation of an anion (R^{-}), typically characterized by the PA value. In the second step, an electron is transferred from the antioxidant anion to stabilize the system. The antioxidant capacity of the chalcones is assessed by calculating their electron transfer enthalpy.

The PA values for each hydrogen atom in the chalcones were determined, and the results are presented in Table 3. According to the data, chalcone 3 has the lowest PA value at the C2–H1 position, measuring 319.17 kcal mol^{-1}. Chalcone 1 also shows its lowest PA value at the

C2–H1 position, recorded at 319.44 kcal mol^{-1}. This indicates that the C–H bonds in chalcone 1 are less favorable for the SPLET mechanism due to their slightly higher PA values, making deprotonation less efficient.

ETE plays a crucial role in the final step of the SPLET mechanism. The calculated ETE values for the chalcones are considerably lower than their IP, indicating that electron transfer from the anionic antioxidant form is more energetically favorable than from the neutral form. This trend aligns with previous research findings [48-49]. The ETE value for the C2–H1 bond in chalcone 3 is significantly higher among the chalcones. This is attributed to forming a double bond between C2 and C3 during the deprotonation step, which increases the molecule's stability and, consequently, the energy required for electron release from the anionic form. Chalcone 3 exhibits enhanced antioxidant activity in both stages of the SPLET mechanism, with a combined PA + ETE value ranging from 420.89 to 422.81 kcal mol^{-1}. Based on the enthalpy calculations for the HAT, SET-PT, and SPLET mechanisms, the HAT pathway is identified as the dominant scavenging mechanism for the chalcones.

Thermodynamics and Energy Barrier of the HAT Mechanism of the Chalcones by •OH Radical

To further investigate the free radical scavenging activity of chalcones 1–3, the energy barriers for the HAT reactions between chalcones 1–3 and the •OH radical in aqueous solution were calculated at M06-2X/6-311G** level of theory with the CPCM solvation model. The •OH radical is commonly used as an appropriate model for assessing antioxidant activity [50]. Also, •OH radical is considered one of the most reactive and toxic free radicals for living organisms [51]. We modelled the HAT reactions from H2 of the chalcones to the •OH radical since the C–H2 bond is the weakest among other C–H bonds, as shown in the previous section.

As illustrated in Fig. 5, the transition states (TS) of chalcones 1–3 interacting with •OH occur via intermolecular H2···OH hydrogen bonds. All HAT reactions of the chalcones by •OH radical proceed via a relatively low energy barrier below 5 kcal/mol. The energy barrier for TS chalcone 3 (TS3) is approximately 3.9 kcal/mol. Similar trends were observed for chalcones 1 and 2; however, their energy barriers are reduced to 1.5 kcal/mol (TS1) and 0.8 kcal/mol (TS2), indicating that the HAT process is faster for chalcone 2 (TS2). Furthermore, the negative reaction enthalpy (ΔH) and Gibbs energy (ΔG) values shown in Table 4 suggest that these reactions are exothermic and thermodynamically favorable. Based on the Gibbs activation energies (ΔG‡), chalcone 3 exhibits higher energy barriers compared to chalcones 1 and 2, indicating that the HAT mechanism proceeds with less energy needed in chalcone 2. The theoretical calculations suggest that the designed chalcones exhibit excellent radical scavenging activity against OH radical in aqueous solution.

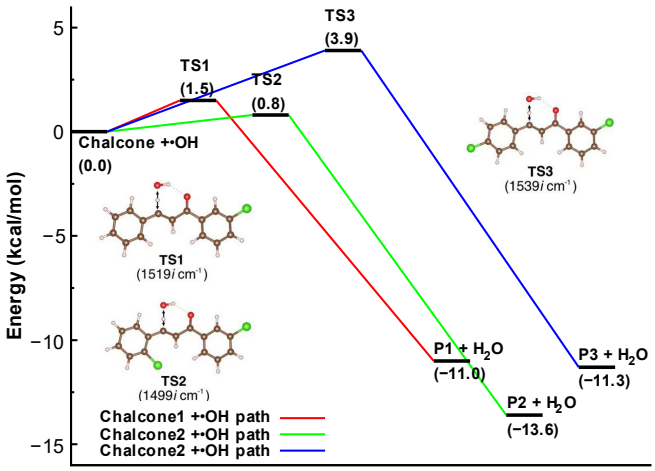

Fig 5. Zero-point energy-corrected diagram of the HAT mechanism between chalcone 1–3 and •OH radical in aqueous solution. The arrows show the movement of the hydrogen atom corresponding to the imaginary (negative) vibrational frequency

Table 4. Relative reaction enthalpies (ΔH) and Gibbs free energies (ΔG), and activation enthalpies (ΔH‡) and Gibbs energies (ΔG‡) for the HAT channel of TS chalcone 1–3 with the •OH radical in the aqueous solution. Thermodynamic corrections are calculated at room temperature (298.15 K). The energies unit is in kcal/mol

Compound	ΔH	ΔG	ΔH‡	ΔG‡
Chalcone 1	−10.7	−11.7	0.6	10.6
Chalcone 2	−13.2	−14.8	−0.1	9.7
Chalcone 3	−10.9	−14.7	3.0	11.4

Frontier Molecular Orbitals

To better understand the chemical reactivity of chalcones 1–3, it is important to examine their electronic characteristics, as these molecules can engage in chemical interactions through the donation or acceptance of electron density. Accordingly, the frontier molecular orbitals (FMOs) were calculated at the M06-2X/6-311++G(*d*,*p*) level of theory in an aqueous medium for each chalcone. The corresponding isosurface representations are shown in Fig. 6. The highest occupied molecular orbital (HOMO) indicates the nucleophilic potential of a molecule, reflecting its tendency to donate electrons during chemical reactions. Conversely, the lowest unoccupied molecular orbital (LUMO) represents the electrophilic nature, highlighting the molecule's ability to accept electrons. Therefore, a comprehensive evaluation of both HOMO and LUMO is essential to elucidate the reactivity patterns of the chalcone derivatives.

As depicted in Fig. 6, the FMO distribution for all three chalcones reveals a consistent spatial pattern. The HOMO is primarily concentrated on ring B, the chlorine substituent, and the olefinic double bond, with a minor contribution from the carbonyl oxygen atom on ring A. This localization highlights the strong π-bonding nature of the HOMO, which is significantly delocalized across the conjugated π-system within these molecular regions. The extensive electron density delocalization indicates a pronounced ability to donate electrons, particularly through the π-system associated with ring B and the chlorine group. This electronic feature enhances the chalcones' potential for charge transfer interactions and likely contributes to their heightened reactivity relative to structurally similar compounds.

The LUMO of the chalcones is broadly delocalized across the entire molecular structure, encompassing rings A and B, the chlorine substituent, the carbonyl moiety, and the olefinic double bond. This spatial distribution aligns with the antibonding regions of the π-system, conferring a distinct π*-antibonding character to the LUMO. Such extensive delocalization indicates that these molecules can accept electron density at multiple sites. Moreover, resonance effects further enhance this uniform electron deficiency, facilitating the stabilization of additional negative charge. This property highlights the chalcones' potential to participate efficiently in electron-accepting interactions, reinforcing their versatility in electron transfer mechanisms.

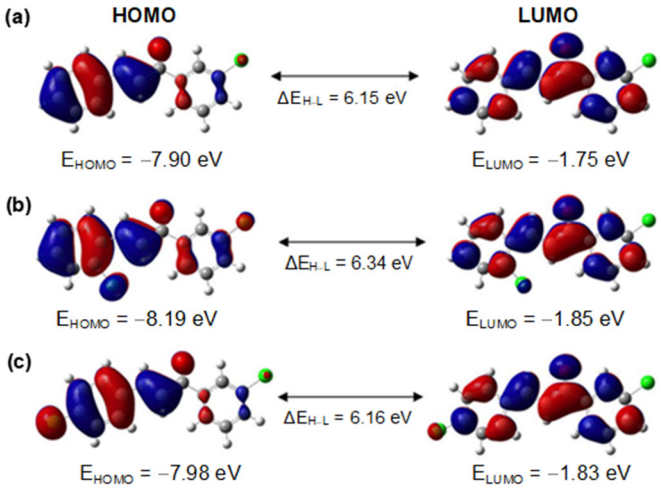

Fig 6. The isosurfaces of the frontier molecular orbitals (FMOs), along with their corresponding orbital energies and the HOMO–LUMO energy gaps, were calculated in water at the M06-2X/6-311++G(*d*,*p*) level for chalcones (a) 1, (b) 2, and (c) 3

Quantum Chemical Reactivity Descriptors

Table 5 presents the global quantum chemical reactivity descriptors for the chalcones, calculated using the M06-2X/6-311++G(*d*,*p*) level of theory. The HOMO–LUMO energy gap (ΔE_{H-L}) is a critical indicator of reactivity, with smaller gaps correlating to higher reactivity due to a stronger interaction between nucleophilic (HOMO) and electrophilic (LUMO) properties. Chalcone 1, with the smallest energy gap (6.15 eV) and the strongest nucleophilic character (HOMO = −7.90 eV), is the most reactive. Chalcone 3, with a slightly larger energy gap (6.16 eV), exhibits balanced nucleophilic and electrophilic properties, making it moderately reactive. In contrast, chalcone 2 has the largest energy gap (6.34 eV) and highest electronegativity (χ = 5.02 eV), but its high hardness renders it the least reactive. The overall reactivity trend is chalcone 1 > chalcone 3 > chalcone 2. These results align with the global hardness, softness, and electrophilicity indices, illustrating how quantum chemical descriptors

Table 5. Global quantum chemical reactivity descriptors calculated at M06-2X/6-311++G(*d*,*p*) level of theory for the chalcones 1–3

Global quantum reactivity descriptors	Chalcone 1	Chalcone 2	Chalcone 3
HOMO energy (E_{HOMO}/eV)	−7.90	−8.19	−7.98
LUMO energy (E_{LUMO}/eV)	−1.75	−1.85	−1.83
Energy gap (ΔE_{H-L}/V)	6.15	6.34	6.16
Ionization potential (IP/eV)	7.90	8.19	7.98
Electron affinity (A/eV)	1.75	1.85	1.83
Electronegativity (χ/eV)	4.83	5.02	4.90
Global hardness (η/eV)	3.08	3.17	3.08
Global softness (σ/eV^{-1})	0.16	0.16	0.16
Electrophilicity index (ε/eV)	0.26	0.25	0.26
Nucleophilicity index (ω/eV^{-1})	3.79	3.97	3.91

effectively explain the reactivity variations among the chalcones.

Molecular Electrostatic Potential

Fig. 7 illustrates the MEP maps for the chalcones, computed using the M06-2X/6-311++G(*d*,*p*) level of theory in the water phase. The MEP map uses color coding to visualize the charge distribution: red regions indicate areas with a negative charge, yellow to orange regions correspond to partially negative charges, green regions represent neutral charges, light blue regions indicate partially positive charges, and blue regions denote positive charges. This color-coded representation provides insights into the chalcones' electron density distribution and potential reactive sites.

The MEP maps for chalcones 1–3, computed at the M06-2X/6-311++G(*d*,*p*) level of theory in the gas phase, reveal consistent MEP distributions with variations stemming from the distinct functional groups in each chalcone. The red regions, concentrated around the oxygen atoms in the carbonyl group, reflect their higher electronegativity and indicate the presence of partial negative charges. Yellow-to-green regions, distributed across the aromatic rings (A and B) and the olefinic double bond, correspond to the π-electron density, inducing partial negative charges on the associated carbon atoms. The hydrogen atom in the hydroxyl group is marked by a blue-colored region, indicating its significant partial positive charge due to its role in hydrogen bonding with the carbonyl oxygen.

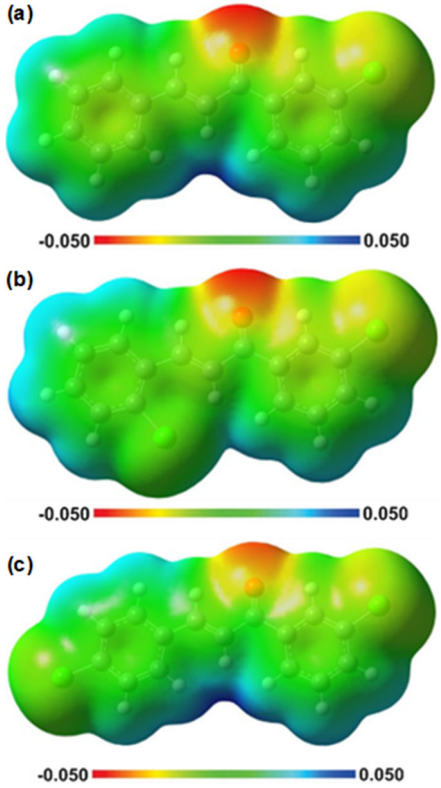

Fig 7. Molecular electrostatic potential (MEP) maps of chalcones (a) 1, (b) 2, and (c) 3 computed in the gas phase at the M06-2X/6-311++G(*d*,*p*) level of theory

Furthermore, the yellow-to-red regions near the chlorine atom highlight its partial negative charge arising from its electronegative nature. These MEP maps effectively demonstrate the charge distribution across the chalcones, providing insights into their electronic characteristics and potential reactive sites. The remaining

hydrogen atoms characteristic of the chalcone skeleton are represented by light blue regions in the MEP maps, indicating partial positive charges due to their proximity to π-electron-dense areas. The green and blue regions within the molecular framework suggest susceptibility to nucleophilic attack, aligning with the LUMO distribution, which is delocalized across the entire molecular structure for all chalcones. The widespread yellow-to-green regions further support the notion of electron density acceptance throughout the structure, consistent with the MEP and LUMO findings. Overall, the MEP maps validate the electronic properties obtained from quantum chemical analyses, effectively highlighting the reactivity and charge distributions within the chalcones.

Vibrational Analyses

As shown in Fig. 8, the chalcones exhibit vibrational spectra consistent with typical experimental findings. In the high-frequency range above 1750 cm^{-1}, the spectra display characteristic absorptions associated with the stretching vibrations of carbon-hydrogen and carbon-carbon bonds [52]. These include individual C–H stretches, symmetric and asymmetric C–H stretches within methyl groups. In the lower frequency region, notable features include bending vibrations of H-C(sp^3)-H bonds and strong absorption bands between 1294 and 1300 cm^{-1}.

ADMET Prediction Analysis

The ADMET (Absorption, Distribution, Metabolism, Excretion, and Toxicity) profiles of the chalcone compounds were further assessed, with the results presented in Table 6. Water solubility is a critical factor influencing drug absorption, particularly for orally administered (enteral) compounds, as hydrophilic drugs are generally more readily absorbed than lipophilic ones. To predict oral bioavailability, the permeability of the compounds was evaluated using the Caco-2 cell model, which serves as an established in vitro representation of the human intestinal epithelium. According to established criteria, compounds with water solubility values below –6 are classified as poorly soluble, while a Caco-2 permeability value exceeding 0.90 indicates high intestinal permeability [53]. Human intestinal absorption (HIA) reflects the gastrointestinal tract's capacity to absorb orally administered substances, with values above 80% considered indicative of good absorption, and those below 30% reflecting poor uptake [54]. The chalcones exhibited favorable pharmacokinetic properties, with water solubility values greater than –6, predicted Caco-2 permeability values exceeding 0.90, and HIA percentages above 90%, collectively suggesting excellent absorption potential.

The steady-state volume of distribution (VDss) reflects a compound's capacity to disseminate throughout the bloodstream and into body tissues following administration. VDss values near –0.15 indicate limited distribution, whereas values exceeding 0.45 are indicative of extensive tissue distribution [55]. Blood-brain barrier (BBB) permeability assesses a compound's ability to traverse the protective membrane surrounding the brain, while central nervous system (CNS) permeability

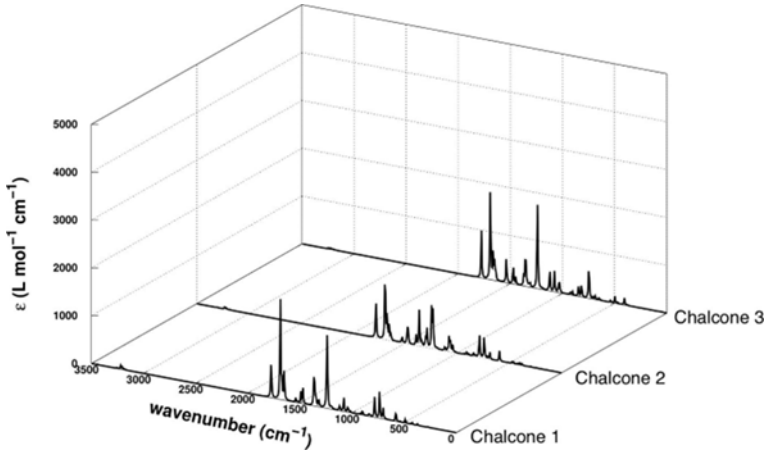

Fig 8. Simulated infrared spectra of the chalcones

Table 6. ADMET prediction of the chalcones

ADMET prediction	Test name	Chalcone		
		1	2	3
Absorption	Water solubility (log mol/L)	−5.045	−5.702	−5.663
	Caco-2 permeability (log Papp in 10^{-6} cm/s)	1.56	1.411	1.408
	Intestinal absorption (human) (% absorbed)	94.308	93.332	92.879
Distribution	VDss (human) (log L/kg)	0.648	0.699	0.665
	BBB permeability (log BB)	0.582	0.587	0.595
	CNS permeability (log PS)	−1.246	−1.243	−1.236
Metabolism	CYP2D6 substrate	No	No	No
	CYP3A4 substrate	Yes	Yes	Yes
	CYP2D6 inhibitor	No	No	No
	CYP3A4 inhibitor	No	No	No
Excretion	Total clearance (log mL/min/kg)	0.067	−0.057	−0.066
	Renal OCT2 substrate	No	No	No
Toxicity	AMES toxicity	No	No	No
	hERG I inhibitor	No	No	No
	hERG II inhibitor	No	No	No
	Oral rat acute toxicity (LD_{50}) (mol/kg)	2.109	2.267	2.269
	Hepatotoxicity	No	No	No

evaluates its potential to access CNS tissues. Effective BBB penetration is associated with log BBB values greater than 0.3, while poor permeability is denoted by values below –1. Similarly, CNS permeability is considered high when log PS values are above –2 and low when below –3 [34]. Chalcones 1–3 exhibit VDss values greater than 0.45, along with log BBB values exceeding 0.3 and log PS values above –2. These findings suggest that the compounds are well-distributed in systemic circulation and possess the ability to cross both the blood-brain barrier and the central nervous system barrier.

Cytochrome P450 is a crucial enzyme predominantly found in the liver, responsible for the oxidative metabolism of xenobiotics, thereby contributing to drug inactivation. This enzyme family includes several isoforms, such as CYP2D6 and CYP3A4, which are key players in the biotransformation of various drugs and xenobiotic compounds [56]. When compounds serve as substrates for these isoforms, it indicates that they are likely to undergo metabolic processing by CYP450. Conversely, compounds that act as inhibitors may interfere with CYP450 activity, potentially affecting drug metabolism. As presented in Table 6, none of the chalcone derivatives function as inhibitors of either CYP2D6 or CYP3A4, suggesting favorable metabolic compatibility with cytochrome P450. In the renal system, the organic cation transporter 2 (OCT2) is located on the basolateral membrane of proximal tubule cells and plays a vital role in the uptake, distribution, and elimination of cationic drugs and endogenous substances [57]. Compounds that are substrates of OCT2 may exhibit adverse interactions with OCT2 inhibitors. Drug excretion is characterized by total clearance values, with lower values indicating a compound's susceptibility to elimination. According to the data in Table 6, none of the chalcones are identified as OCT2 substrates, and all exhibit high total clearance values, indicating efficient elimination profiles.

Furthermore, toxicity profile analysis reveals that none of the chalcones demonstrate carcinogenic potential. Additionally, their acute oral toxicity is within a safe range, and they do not exhibit hepatotoxic effects, confirming that these compounds are relatively non-toxic and safe for further pharmacological consideration.

■ CONCLUSION

Chalcones 1–3 were efficiently synthesized via ultrasound-assisted methods, achieving high yields (> 80%) and shorter reaction times. Antioxidant activity

was confirmed through DPPH and ABTS assays. All compounds showed excellent UV-B and UV-A filtering capabilities, with chalcone 3 exhibiting the highest SPF (19.47 ± 0.46) at 20 ppm. ADMET analysis indicated favorable pharmacokinetics, including good absorption, distribution, and low toxicity.

Furthermore, computational studies on the hydrogen atom transfer (HAT) mechanism with the hydroxyl radical (•OH) demonstrated low activation energy barriers and exergonic thermodynamics, confirming the chalcones' efficient and spontaneous radical scavenging capacity. These mechanistic insights align with experimental antioxidant results, reinforcing their suitability as effective radical scavengers for biological and cosmetic applications.

This comprehensive study, integrating experimental and computational approaches, highlights chlorochalcone derivatives as promising multifunctional agents with potent antioxidant activity, strong UV protection, and favorable pharmacokinetic profiles—making them ideal candidates for innovative, sustainable skincare formulations targeting oxidative stress and photodamage.

■ ACKNOWLEDGMENTS

The Ministry of Research, Technology, and Higher Education of the Republic of Indonesia, via the *Penelitian Fundamental Reguler* scheme (PFR, Contract No.108/E5/PG.02.00.PL/2024), is acknowledged for the financial support. The calculations were partly performed at BRIN's Mahameru High-Performance Computing. We would also like to thank Mr. Aulia Sukma Hutama from the Department of Chemistry, Faculty of Mathematics and Natural Sciences, Universitas Gadjah Mada, for his help and input in writing this research article.

■ CONFLICT OF INTEREST

The authors have no relevant financial or non-financial interests to disclose.

■ AUTHOR CONTRIBUTIONS

Anita Dwi Puspitasari: Conceptualization, Supervision, Investigation, Writing – review & editing, Validation, Writing – review & editing, Funding acquisition. Lala Adetia Marlina: Visualization, Writing – review & editing, Methodology. Maria Ulfah: Validation, Writing – review & editing. Indah Hartati: Methodology, Investigation, Formal analysis, Writing - original draft & review & editing. Rissa Laila Vifta: Validation, Writing – review & editing. All authors have read and agreed to the final version of this manuscript.

■ REFERENCES

[1] Papaccio, F., D'Arino, A., Caputo, S., and Bellei, B., 2022, Focus on the contribution of oxidative stress in skin aging, *Antioxidants*, 11 (6), 1121.

[2] Bernerd, F., Passeron, T., Castiel, I., and Marionnet, C., 2022, The damaging effects of long UVA (UVA1) rays: A major challenge to preserve skin health and integrity, *Int. J. Mol. Sci*., 23 (15), 8243.

[3] Bowers, J.M., Hamilton, J.G., Lobel, M., Kanetsky, P.A., and Hay, J.L., 2021, Sun exposure, tanning behaviors, and sunburn: Examining activities associated with harmful ultraviolet radiation exposures in college students, *J. Primary Prev.*, 42 (5), 425–440.

[4] Cho, Y.H., Kim, S.Y., Woo, H.D., Kim, Y.J., Ha, S.W., and Chung, H.W., 2015, Delayed numerical chromosome aberrations in human fibroblasts by low dose of radiation, *Int. J. Environ. Res. Public Health*, 12 (12), 15162–15172.

[5] Toriyama, E., Masuda, H., Torii, K., Ikumi, K., and Morita, A., 2021, Time kinetics of cyclobutane pyrimidine dimer formation by narrowband and broadband UVB irradiation, *J. Dermatol. Sci*., 103, 151–155.

[6] Smijs, T.G., and Pavel, S., 2011, Titanium dioxide and zinc oxide nanoparticles in sunscreens: Focus on their safety and effectiveness, *Nanotechnol. Sci*., 4, 95–112.

[7] Baker, L.A., Marchetti, B., Karsili, T.N.V., Stavros, V.G., and Ashfold, M.N.R., 2017, Photoprotection: Extending lessons learned from studying natural sunscreens to the design of artificial sunscreen constituents, *Chem. Soc. Rev*., 46 (12), 3770–3791.

[8] Baker, L.A., Greenough, S.E., and Stavros, V.G., 2016, A perspective on the ultrafast photochemistry

of solution-phase sunscreen molecules, *J. Phys. Chem. Lett*., 7 (22), 4655–4665.

[9] Ramos, S., Homem, V., Alves, A., and Santos, L., 2015, Advances in analytical methods and occurrence of organic UV-filters in the environment — A review, *Sci. Total Environ*., 526, 278–311.

[10] Jesus, A., Mota, S., Torres, A., Cruz, M.T., Sousa, E., Almeida, I.F., and Cidade, H., 2023, Antioxidants in sunscreens: Which and what for?, *Antioxidants*, 12 (1), 138.

[11] Aguiar, A.S.N., Dias, P.G.M., Queiroz, J.E., Firmino, P.P., Custódio, J.M.F., Dias, L.D., Aquino, G.L.B., Camargo, A.J., and Napolitano, H.B., 2023, Insights on potential photoprotective activity of two butylchalcone derivatives: Synthesis, spectroscopic characterization and molecular modeling, *Photonics,* 10 (3), 228.

[12] Mittal, A., Vashistha, V.K., and Das, D.K., 2022, Recent advances in the antioxidant activity and mechanisms of chalcone derivatives: A computational review, *Free Radic. Res*., 56 (5-6), 378–397.

[13] Wijayanti, L.W., Swasono, R.T., Lee, W., and Jumina, J., 2021, Synthesis and evaluation of chalcone derivatives as novel sunscreen agent, *Molecules*, 26 (9), 2698.

[14] Zainuri, D.A., Abdullah, M., Arshad, S., Abd Aziz, M.S., Krishnan, G., Bakhtiar, H., and Abdul Razak, I., 2018, Crystal structure, spectroscopic and third-order nonlinear optical susceptibility of linear fused ring dichloro-substituent chalcone isomers, *Opt. Mater.*, 86, 32–45.

[15] Głębocka, A., Raczyńska, E.D., Chylewska, A., and Makowski, M., 2016, Experimental (FT-IR) and theoretical (DFT) studies on prototropy and H-bond formation for pyrazine-2-amidoxime, *J. Phys. Org. Chem*., 29, 326–335.

[16] Wachter, N.M., Rani, N., Zolfaghari, A., Tarbox, H., and Mazumder, S., 2020, DFT investigations of the unusual reactivity of 2-pyridinecarboxaldehyde in base-catalyzed aldol reactions with acetophenone, *J. Phys. Org. Chem*., 33 (5), e4048.

[17] Tri Suma, A.A., Dwi Wahyuningsih, T., and Mustofa, M., 2019, Efficient synthesis of chloro chalcones under ultrasound irradiation, their anticancer activities and molecular docking studies*, Rasayan J. Chem*., 12 (2), 502–510.

[18] Deshmukh, N., and Shinde, A., 2021, An efficient, ultrasound induced ring closure of hydroxy chalcone in 2-ethoxy ethanol as an green reaction medium and study of antimicrobial potential, *Chem. Data Collect*., 31, 100606.

[19] Hutama, A.S., Huang, H., and Kurniawan, Y.S., 2019, Investigation of the chemical and optical properties of halogen-substituted *N*-methyl-4-piperidone curcumin analogs by density functional theory calculations, *Spectrochim. Acta, Part A*, 221, 117152.

[20] López, G., Mellado, M., Werner, E., Said, B., Godoy, P., Caro, N, Besoain, X, Montenegro, I., and Madrid, A., 2020, Sonochemical synthesis of 2'-hydroxy-chalcone derivatives with potential anti-oomycete activity, *Antibiotics*, 9 (9), 576.

[21] Sayre, R.M., Agin, P.P., LeVee, G.J., and Marlowe, E., 1979, A comparison of *in vivo* and *in vitro* testing of sunscreening formulas, *Photochem. Photobiol*., 29 (3), 559–566.

[22] Frisch, M.J., Trucks, G.W., Schlegel, H.B., Scuseria, G.E., Robb, M.A., Cheeseman, J.R., Scalmani, G., Barone, V., Mennucci, B., Petersson, G.A., Nakatsuji, H., Caricato, M., Li, X., Hratchian, H.P., Izmaylov, A.F., Bloino, J., Zheng, G., Sonnenberg, J.L., Hada, M., Ehara, M., Toyota, K., Fukuda, R., Hasegawa, J., Ishida, M., Nakajima, T., Honda, Y., Kitao, O., Nakai, H., Vreven, T., Montgomery, J.A., Jr., Peralta, J.E., Ogliaro, F., Bearpark, M., Heyd, J.J., Brothers, E., Kudin, K.N., Staroverov, V.N., Kobayashi, R., Normand, J., Raghavachari, K., Rendell, A., Burant, J.C., Iyengar, S.S., Tomasi, J., Cossi, M., Rega, N., Millam, J.M., Klene, M., Knox, J.E., Cross, J.B., Bakken, V., Adamo, C., Jaramillo, J., Gomperts, R., Stratmann, R.E., Yazyev, O., Austin, A.J., Cammi, R., Pomelli, C., Ochterski, J.W., Martin, R.L., Morokuma, K., Zakrzewski, V.G., Voth, G.A., Salvador, P., Dannenberg, J.J., Dapprich, S., Daniels, A.D., Farkas, Ö., Foresman, J.B., Ortiz, J.V., Cioslowski, J., and Fox, D.J., 2013, *Gaussian-09 Revision D.01*, Gaussian, Inc., Wallingford, CT.

[23] Zhao, Y., and Truhlar, D.G., 2008, The M06 suite of density functionals for main group thermochemistry, thermochemical kinetics, noncovalent interactions, excited states, and transition elements: Two new functionals and systematic testing of four M06-class functionals and 12 other functionals, *Theor. Chem. Acc.*, 120 (1), 215–241.

[24] Hehre, W.J., 1976, Ab initio molecular orbital theory, *Acc. Chem. Res.*, 9 (11), 399–406.

[25] Xue, Y., Zheng, Y., An, L., Dou, Y., and Liu, Y., 2014, Density functional theory study of the structure–antioxidant activity of polyphenolic deoxybenzoins, *Food Chem.*, 151, 198–206.

[26] Zheng, Y.Z., Deng, G., Liang, Q., Chen, D.F, Guo, R., and Lai, R.C., 2017, Antioxidant activity of quercetin and its glucosides from propolis: a theoretical study, *Sci. Rep.*, 7 (1), 7543.

[27] Boli, L.S.P., Aisyah, N.D., Khoirunisa, V., Rachmawati, H., Dipojono, H.K., and Rusydi, F., 2019, Solvent effect on bond dissociation enthalpy (BDE) of tetrahydrocurcumin: A theoretical study, *Mater. Sci. Forum*, 966, 215–221.

[28] Nikšić-Franjić, I., and Ljubić, I., 2021, Comparing the performances of various density functionals for modelling the mechanisms and kinetics of bimolecular free radical reactions in aqueous solution, *Phys. Chem. Chem. Phys.*, 21 (42), 23425–23440

[29] Barone, V., and Cossi, M., 1998, Quantum calculation of molecular energies and energy gradients in solution by a conductor solvent model, *J. Phys. Chem. A*, 102 (11), 1995–2001.

[30] Rimarčík, J., Lukeš, V., Klein, E., and Ilčin, M., 2010, Study of the solvent effect on the enthalpies of homolytic and heterolytic N–H bond cleavage in *p*-phenylenediamine and tetracyano-*p*-phenylenediamine, *J. Mol. Struct.: THEOCHEM*, 952 (1), 25–30.

[31] Szeląg, M., Urbaniak, A., and Bluyssen, H.A.R., 2015, A theoretical antioxidant pharmacophore for natural hydroxycinnamic acids, *Open Chem.*, 13 (1), 17–31.

[32] Huang, Y., Rong, C., Zhang, R., and Liu, S., 2016, Evaluating frontier orbital energy and HOMO/LUMO gap with descriptors from density functional reactivity theory, *J. Mol. Model.*, 23 (1), 3.

[33] Marlina, L.A., Hutama, A.S., Arief, I., Mazaya, M., Syafarina, I., and Saputri, W.D., 2024, Exploring the potential of metalloporphyrin-like C54N4 fullerene (TM-PC60F) nanoclusters as new drug delivery platform for 5-fluorouracil: A DFT and QTAIM study, *Diamond Relat. Mater.*, 147, 111267.

[34] Pires, D.E.V., Blundell, T.L., and Ascher, D.B., 2015, pkCSM: Predicting small-molecule pharmacokinetic and toxicity properties using graph-based signatures, *J. Med. Chem.*, 58 (9), 4066–4072.

[35] Myung, Y., de Sá, A.G.C., and Ascher, D.B., 2024, Deep-PK: Deep learning for small molecule pharmacokinetic and toxicity prediction, *Nucleic Acid Res.*, 52 (W1), W469-W475.

[36] Seck, S., Hamad, J., Schalka, S., and Lim, H.W., 2023, Photoprotection in skin of color, *Photochem. Photobiol. Sci.*, 22 (2), 441–456.

[37] Nasihun, T., and Widayati, E., 2018, *Pimpinella alpina* Molk administration is capable of increasing antioxidant and decreasing prooxidant level following UVB irradiation, *J. Nat. Rem.*, 18 (1), 29–39.

[38] Abdlaty, R., Hayward, J., Farrell, T., and Fang, Q., 2021, Skin erythema and pigmentation: A review of optical assessment techniques, *Photodiagn. Photodyn. Ther.*, 33, 102127.

[39] Abdassah, M., Aryani, R., Surachman, E., and Muchtaridi, M., 2015, *In-vitro* assessment of effectiveness and photostability avobenzone in cream formulations by combination ethyl ascorbic acid and alpha tocopherol acetate, *J. Appl. Pharm. Sci.*, 5 (6), 70–74.

[40] Shanbhag, S., Nayak, A., Narayan, R., and Nayak, U.G., 2019, Anti-aging and sunscreens: Paradigm shift in cosmetics, *Adv. Pharm. Bull.*, 9 (3), 348–359.

[41] Farooq, S., Mazhar, A., Ihsan-Ul-Haq, and Ullah, N., 2020, One-pot multicomponent synthesis of novel 3,4-dihydro-3-methyl-2(1*H*)-quinazolinone derivatives and their biological evaluation as potential antioxidants, enzyme inhibitors,

antimicrobials, cytotoxic and anti-inflammatory agents, *Arabian J. Chem*., 13, 9145–9165.

[42] Pandithavidana, D.R., and Jayawardana, S.B., 2019, Comparative study of antioxidant potential of selected dietary vitamins; Computational insights, *Molecules*, 24 (9), 1646.

[43] Tao, Y., Zhang, H., and Wang, Y., 2023, Revealing and predicting the relationship between the molecular structure and antioxidant activity of flavonoids, *LWT*, 174, 114433.

[44] Deshlahra, P., and Iglesia, E., 2016, Reactivity and selectivity descriptors for the activation of C–H bonds in hydrocarbons and oxygenates on metal oxides, *J. Phys. Chem. C*, 120 (30), 16741–16760.

[45] Vo, Q.V., Thi Hoa, N., and Mechler, A., 2023, The hydroperoxyl antiradical activity of natural chalcones in physiological environments: Theoretical insights into the mechanism, kinetics and pH effects, *J. Mol. Liq.*, 383, 122193.

[46] Borgohain, R., Guha, A.K., Pratihar, S., and Handique, J.G., 2015, Antioxidant activity of some phenolic aldehydes and their diimine derivatives: A DFT study, *Comput. Theor. Chem.*, 1060, 17–23.

[47] Borges, R.S., Aguiar, C.P.O., Oliveira, N.L.L., Amaral, I.N.A., Vale, J.K.L., Chaves Neto, A.M.J., Queiroz, A.N., and da Silva, A.B.F., 2023, Antioxidant capacity of simplified oxygen heterocycles and proposed derivatives by theoretical calculations, *J. Mol. Model.*, 29 (8), 232.

[48] Thong, N.M, Quang, D.T., Bui, N.H.T., Dao, D.Q., and Nam, P.C., 2015, Antioxidant properties of xanthones extracted from the pericarp of *Garcinia mangostana* (Mangosteen): A theoretical study, *Chem. Phys. Lett*., 625, 30–35.

[49] Li, M., Liu, W., Peng, C., Ren, Q., Lu, W., and Deng, W., 2013, A DFT study on reaction of eupatilin with hydroxyl radical in solution, *Int. J. Quantum Chem.*, 113 (7), 966–974.

[50] Tumilaar, S.G., Hardianto, A., Dohi, H., and Kurnia, D., 2024, A comprehensive review of free radicals, oxidative stress, and antioxidants: Overview, clinical applications, global perspectives, future directions, and mechanisms of antioxidant activity of flavonoid compounds, *J. Chem*., 2024 (1), 5594386.

[51] Lipinski, B., 2011, Hydroxyl radical and its scavengers in health and disease, *Oxid. Med. Cell. Longevity*, 2011 (1), 809696.

[52] Socrates, G., 2001, *Infrared and Raman Characteristic Group Frequencies*, John Wiley & Sons, Chichester.

[53] Petrescu, A.M., Paunescu, V., and Ilia, G., 2019, The antiviral activity and cytotoxicity of 15 natural phenolic compounds with previously demonstrated antifungal activity, *J. Environ. Sci. Health, Part B*, 54 (6), 498–504.

[54] Wang, N.N., Huang, C., Dong, J., Yao, Z.J., Zhu, M.F., Deng, Z.K., Lv, B., Lu, A.P., Chen, A.F., and Cao, D.S., 2017, Predicting human intestinal absorption with modified random forest approach: a comprehensive evaluation of molecular representation, unbalanced data, and applicability domain issues, *RSC Adv*., 7 (31), 19007–19018.

[55] Lombardo, F., Bentzien, J., Berellini, G., and Muegge, I., 2021, *In silico* models of human PK parameters. Prediction of volume of distribution using an extensive data set and a reduced number of parameters, *J. Pharm. Sci.*, 110 (1), 500–509.

[56] Basheer, L., and Kerem, Z., 2015, Interactions between CYP3A4 and dietary polyphenols, *Oxid. Med. Cell. Longevity*, 2015 (1), 854015.

[57] Shen, Q., Wang, J., Yuan, Z., Jiang, Z., Shu, T., Xu, D., He, J., Zhang, L., and Huang, X., 2019, Key role of organic cation transporter 2 for the nephrotoxicity effect of triptolide in rheumatoid arthritis, *Int. Immunopharmacol.*, 77, 105959.